

1 **A novel method for calculating ambient aerosol**
2 **liquid water contents based on measurements of a**
3 **humidified nephelometer system**

4 **Ye Kuang¹, ChunSheng Zhao², Gang Zhao², JiangChuan Tao¹, Wanyun Xu³, Nan Ma¹,**
5 **YuXuan Bian³**

6 [1]{Institute for Environmental and Climate Research, Jinan University, Guangzhou 511443,
7 China}

8 [2]{Department of Atmospheric and Oceanic Sciences, School of Physics, Peking University,
9 Beijing, China}

10 [3]{State Key Laboratory of Severe Weather, Chinese Academy of Meteorological Sciences}

11

12 Correspondence to: C. S. Zhao (zcs@pku.edu.cn)

13 **Abstract**

14 Water condensed on ambient aerosol particles plays significant roles in atmospheric
15 environment, atmospheric chemistry and climate. So far, no instruments were available for real-
16 time monitoring of ambient aerosol liquid water contents (ALWC). In this paper, a novel method

17 is proposed to calculate ambient ALWC based on measurements of a three-wavelength humidified
18 nephelometer system, which measures aerosol light scattering coefficients and backscattering
19 coefficients at three wavelengths under dry state and different relative humidity (RH) conditions,
20 providing measurements of light scattering enhancement factor $f(\text{RH})$. The proposed ALWC
21 calculation method includes two steps. The first step is the estimation of the dry state total volume
22 concentration of ambient aerosol particles, $V_a(\text{dry})$, with a machine learning method called
23 random forest model based on measurements of the “dry” nephelometer. The estimated $V_a(\text{dry})$
24 agrees well with the measured one. The second step is the estimation of the volume growth factor
25 $V_g(\text{RH})$ of ambient aerosol particles due to water uptake, using $f(\text{RH})$ and Ångström exponent.
26 The ALWC is calculated from the estimated $V_a(\text{dry})$ and $V_g(\text{RH})$. To validate the new method,
27 the ambient ALWC calculated from measurements of the humidified nephelometer system during
28 the Gucheng campaign was compared with ambient ALWC calculated from ISORROPIA
29 thermodynamic model using aerosol chemistry data. A good agreement was achieved, with a slope
30 and intercept of 1.14 and $-8.6 \mu\text{m}^3/\text{cm}^3$ ($r^2=0.92$), respectively. The advantage of this new method
31 is that the ambient ALWC can be obtained solely based on measurements of a three-wavelength
32 humidified nephelometer system, facilitating the real-time monitoring of the ambient ALWC and
33 promoting the study of aerosol liquid water and its role in atmospheric chemistry, secondary
34 aerosol formation and climate change.

35

36 **1. Introduction**

37 Atmospheric aerosol particles play significant roles in atmospheric environment, climate,
38 human health and the hydrological cycle, and have received much attention in recent decades. One

39 of the most important constituents of ambient atmospheric aerosol is liquid water. The content of
40 condensed water on ambient aerosol particles depends mostly on the aerosol hygroscopicity and
41 the ambient relative humidity (RH). Results of previous studies demonstrate that liquid water
42 contributes greatly to the total mass of ambient aerosol particles when the ambient RH is higher
43 than 60% (Bian et al., 2014). Aerosol liquid water also has large impacts on aerosol optical
44 properties and aerosol radiative effects (Tao et al., 2014;Kuang et al., 2016). Liquid water
45 condensed on aerosol particles can also serves as a site for multiphase reactions which perturb
46 local chemistry and further influence the aging processes of aerosol particles (Martin, 2000).
47 Recent studies have shown that aerosol liquid water serves as a reactor, which can efficiently
48 transform sulphur dioxide to sulphate during haze events, aggravating atmospheric environment
49 in the North China Plain (NCP) (Wang et al., 2016;Cheng et al., 2016). Hence, to gain more insight
50 into the role of aerosol liquid water in atmospheric chemistry, aerosol aging processes and aerosol
51 optical properties, the real-time monitoring of ambient aerosol liquid water content (ALWC) is of
52 crucial importance..

53 Few techniques are currently available for measuring the ALWC. The humidified tandem
54 differential mobility analyser systems (HTDMAs) are useful tools and widely used to measure
55 hygroscopic growth factors of ambient aerosol particles (Rader and McMurry, 1986;Wu et al.,
56 2016;Meier et al., 2009). Hygroscopicity parameters retrieved from measurements of HTDMAs
57 can be used to calculate the volume of liquid water. Nevertheless, HTDMAs cannot be used to
58 measure the total aerosol water volume, because they are not capable of measuring the hygroscopic
59 properties of the entire aerosol population. With size distributions of aerosol particles in their
60 ambient state and dry state, the aerosol water volume can be estimated. Engelhart et al. (2011)
61 deployed a Dry-Ambient Aerosol Size Spectrometer to measure the aerosol liquid water content

62 and volume growth factor of fine particulate matter. This system provides only aerosol water
63 content of aerosol particles within certain size range (particle diameter less than 500 nm for the
64 setup of Engelhart et al. (2011)). In addition, in conjunction with aerosol thermodynamic
65 equilibrium models, ALWC can also be estimated with detailed aerosol chemical information.
66 However, simulations of aerosol hygroscopicity and phase state by using thermodynamic
67 equilibrium models are still very complicated even under the thermodynamic equilibrium
68 hypothesis and these models may cause large bias when used for estimating ALWC (Bian et al.,
69 2014).

70 The idea of using the humidified nephelometer system for the study of aerosol hygroscopicity
71 has already been proposed very early on (Covert et al., 1972). The instrument measures aerosol
72 light scattering coefficient (σ_{sp}) under dry state and different RH conditions, providing
73 information on aerosol light scattering enhancement factor $f(RH)$. One advantage of this method
74 is that it has a fast response time and continuous measurements can be made, facilitating the
75 monitoring of changes in ambient conditions. Another advantage of this method is that it provides
76 information on the overall aerosol hygroscopicity of the entire aerosol population (Kuang et al.,
77 2017a). Both measured σ_{sp} of aerosol particles in dry state and $f(RH)$ vary strongly with
78 parameters of particle number size distribution (PNSD), making it difficult to directly link them
79 with the dry state aerosol particle volume ($V_a(\text{dry})$) and the volume growth factor $Vg(RH)$ of the
80 entire aerosol population. So far, the ALWC could not be directly estimated based solely on
81 measurements of the humidified nephelometer system. Several studies have shown that given the
82 PNSDs at dry state, an iterative algorithm together with the Mie theory can be used to calculate an
83 overall aerosol hygroscopic growth factor $g(RH)$ based on measurements of $f(RH)$ (Zieger et al.,
84 2010; Fierz-Schmidhauser et al., 2010). In such an iterative algorithm, the $g(RH)$ is assumed to be

85 independent of the aerosol diameter. Then ALWC at different RH levels can be calculated based
86 on derived $g(\text{RH})$ and the measured PNSD. This method not only requires additional
87 measurements of PNSD, but also may result in significant deviations of the estimated ALWC,
88 because $g(\text{RH})$ should be a function of aerosol diameter rather than a constant value. Another
89 method, which directly connects $f(\text{RH})$ to $Vg(\text{RH})$ ($Vg(\text{RH}) = f(\text{RH})^{1.5}$), is also used for
90 predicting ALWC based on measurements of the humidified nephelometer system and mass
91 concentrations of dry aerosol particles (Guo et al., 2015). This method assumes that the average
92 scattering efficiency of aerosol particles at dry state and different RH conditions are the same, and
93 requires additional measurements of PNSD or mass concentrations of dry aerosol particles (Guo
94 et al., 2015). However, the scattering efficiency of aerosol particles vary with particle diameters,
95 which will change under ambient conditions due to aerosol hygroscopic growth.

96 In this paper, we propose a novel method to calculate the ALWC based only on
97 measurements of a humidified nephelometer system. The proposed method includes two steps.
98 The first step is calculating $V_a(\text{dry})$ based on measurements of the “dry” nephelometer using a
99 machine learning method called random forest model. With measurements of PNSD and BC, the
100 six parameters measured by the nephelometer can be simulated using the Mie theory, and the
101 $V_a(\text{dry})$ can also be calculated based on PNSD. Therefore, the random forest model can be trained
102 with only regional historical datasets of PNSD and BC. The second step is calculating $Vg(\text{RH})$
103 based on the Ångström exponent and $f(\text{RH})$ measured by the humidified nephelometer system.
104 In this step, both the influences of the variations in PNSD and aerosol hygroscopicity are both
105 taken into account to derive $Vg(\text{RH})$ from measured $f(\text{RH})$. Finally, based on calculated $V_a(\text{dry})$
106 and $Vg(\text{RH})$, ALWCs at different RH points can be estimated. The used datasets are introduced in
107 Sect.2. Calculation method of $V_a(\text{dry})$ based only on measurements of the nephelometer, which

108 measures optical properties of aerosols in dry state, is described in Sect.3.2. The way of deriving
109 $V_g(\text{RH})$ based on measurements of the humidified nephelometer system is introduced and
110 discussed in Sect.3.3. The final formula of calculating ambient ALWC is described in Sect.3.4.
111 The verification of the $V_a(\text{dry})$ predicted by using the machine learning method is described in
112 Sect.4.1. The validation of ambient ALWC calculated from measurements of the humidified
113 nephelometer system is presented in Sect.4.2. The contribution of ambient ALWC to the total
114 ambient aerosol volume is discussed in Sect.4.3.

115 **2. Instruments and datasets**

116 Datasets from six field campaigns were used in this paper. The six campaigns were conducted
117 at four different measurement sites (Wangdu, Gucheng and Xianghe in Hebei province and
118 Wuqing in Tianjin) of the North China Plain (NCP), the locations of these field campaign sites are
119 displayed in Fig.S1. Time periods and datasets used from these field campaigns are listed in Table
120 1. During these field campaigns, aerosol particles with aerodynamic diameters less than $10\ \mu\text{m}$
121 were sampled (by passing through an impactor). The PNSDs in dry state, which range from 3nm
122 to $10\ \mu\text{m}$, were jointly measured by a Twin Differential Mobility Particle Sizer (TDMPS, Leibniz-
123 Institute for Tropospheric Research, Germany; Birmili et al. (1999)) or a scanning mobility
124 particle size spectrometer (SMPS) and an Aerodynamic Particle Sizer (APS, TSI Inc., Model 3321)
125 with a temporal resolution of 10 minutes. The mass concentrations of black carbon (BC) were
126 measured using a Multi-Angle Absorption Photometer (MAAP Model 5012, Thermo, Inc.,
127 Waltham, MA USA) with a temporal resolution of 1 minute during field campaigns of F1 to F5,
128 and using an aethalometer (AE33) (Drinovec et al., 2015) during field campaign F6. The aerosol
129 light scattering coefficients (σ_{sp}) at three wavelengths (450 nm, 550 nm, and 700 nm) were

130 measured using a TSI 3563 nephelometer (Anderson and Ogren, 1998) during field campaigns of
131 F1 to F5, and using an Aurora 3000 nephelometer (Müller et al., 2011) during field campaign F6.

132 Datasets of PNSD, BC and σ_{sp} from campaigns F2, F4 and F5 are referred to as D1.
133 Measurements of PNSD and measurements from the humidified nephelometer system during
134 campaign F6 (Gucheng campaign) are used to verify the proposed method of calculating the
135 ambient ALWC. Details about the humidified nephelometer system during Wangdu and Gucheng
136 campaigns are introduced in detail in (Kuang et al., 2017a). During the Gucheng campaign, an In
137 situ Gas and Aerosol Compositions Monitor (IGAC, Fortelice International Co., Taiwan) was used
138 for monitoring water-soluble ions (Na^+ , K^+ , Ca^{2+} , Mg^{2+} , NH_4^+ , SO_4^{2-} , NO_3^- , Cl^-) of $\text{PM}_{2.5}$ and their
139 precursor gases: NH_3 , HCl , and HNO_3 . The time resolution of IGAC measurements is one hour.
140 Ambient air was drawn into the IGAC system through a stainless steel pipe wrapped with thermal
141 insulation at a flow rate of 16.7 L/min. The ambient RH and temperature were observed using an
142 automatic weather station with a time resolution of one minute.

143 3. Methodology

144 3.1 Closure calculations

145 To ensure the datasets of σ_{sp} and PNSD used are of high quality, a closure study between
146 measured σ_{sp} and that calculated based on measured PNSD and BC with Mie theory (Bohren and
147 Huffman, 2008) is first performed. Measured σ_{sp} bears uncertainties introduced by angular
148 truncation errors and nonideal light source. To achieve consistency between measured and
149 modelled σ_{sp} , modelled σ_{sp} are calculated according to practical angular situations of the
150 nephelometer (Anderson et al., 1996). During the σ_{sp} modelling process, BC was considered to

151 be half externally and half coreshell mixed with other aerosol components. The mass size
152 distribution of BC used in Ma et al. (2012), which was also observed in the NCP, was used in this
153 research to account for the mass distributions of BC at different particle sizes. The applied
154 refractive index and density of BC were $1.80 - 0.54i$ and 1.5g cm^{-3} (Kuang et al., 2015). The
155 refractive index of non light-absorbing aerosol components (other than BC) was set to $1.53 -$
156 $10^{-7}i$ (Wex et al., 2002). For the Mie theory calculation details please refer to Kuang et al. (2015).

157 The closure results between modelled σ_{sp} and σ_{sp} measured by TSI 3563 or Aurora 3000
158 using datasets observed during six field campaigns (Table 2) are depicted in Fig.1. In general, for
159 all six field campaigns, modelled σ_{sp} values correlate very well with measured σ_{sp} values.
160 Considering the measured PNSD has an uncertainty of larger than 10% (Wiedensohler et al., 2012),
161 and the measured σ_{sp} has an uncertainty of about 9% (Sherman et al., 2015), modelled σ_{sp} values
162 agree well with measured σ_{sp} values in campaigns F1, F4, F5 and F6, with all points lying nearby
163 the 1:1 line, and most points falling within the 20% relative difference lines. For the closure results
164 of field campaign F2, the modelled σ_{sp} values are systematically lower than measured σ_{sp} values.
165 For the closure results of field campaign F3, most points also lie nearby 1:1 line, but points are
166 relatively more dispersed.

167 **3.2 Calculation of V_a (dry) based on measurements of the “dry” nephelometer**

168 **3.2.1 Theoretical relationship between V_a (dry) and σ_{sp}**

169 Previous studies demonstrated that the σ_{sp} of aerosol particles is roughly proportional to
170 V_a (dry) (Pinnick et al., 1980). Here, the quantitative relationship between V_a (dry) and σ_{sp} is
171 analyzed.

172 The σ_{sp} and $V_a(\text{dry})$ can be expressed as the following:

173
$$\sigma_{sp} = \int \pi r^2 Q_{sca}(m, r) n(r) dr \quad (1)$$

174
$$V_a(\text{dry}) = \int \frac{4}{3} \pi r^3 n(r) dr \quad (2)$$

175 where $Q_{sca}(m, r)$ is scattering efficiency for a particle with refractive index m and particle radius
176 r , while $n(r)$ is the aerosol size distribution. As presented in equation (1) and (2), relating $V_a(\text{dry})$
177 with σ_{sp} involves the complex relation between $Q_{sca}(m, r)$ and particle diameter, which can be
178 simulated using the Mie theory. According to the aerosol refractive index at visible spectral range,
179 aerosol chemical components can be classified into two categories: the light absorbing component
180 and the almost light non-absorbing components (inorganic salts and acids, and most of the organic
181 compounds). Near the visible spectral range, the light absorbing component can be referred to as
182 BC. BC particles are neither externally nor internally mixed with other aerosol components. In
183 view of this, Q_{sca} at 550 nm as a function of particle diameter for four types of aerosol particles is
184 simulated using Mie theory: almost non-absorbing aerosol particle, BC particle, BC particle core-
185 shell mixed with non-absorbing components with the radius of the inner BC core being 50 nm and
186 70 nm, respectively. Same with those introduced in Sect.2.2, the refractive indices of BC and light
187 non-absorbing components used here are $1.80 - 0.54i$ and $1.53 - 10^{-7}i$, respectively.

188 The simulated results are shown in Fig.2a. Near the visible spectral range, most of the ambient
189 aerosol components are almost non-absorbing, and their Q_{sca} varies more like the blue line shown
190 in Fig.2a. In that case, aerosol particles have diameters less than about 800 nm and Q_{sca} increases
191 almost monotonously with particle diameter and can be approximately estimated as a linear
192 function of diameter. Fig.2b shows the simulated size-resolved accumulative contribution to the
193 scattering coefficient at 550 nm for all PNSDs measured during the Wangdu campaign. The results

194 indicate that, for continental aerosol particles without influences of dust, in most cases, all particles
195 with diameter less than about 800 nm contribute more than 80% to the total σ_{sp} . Therefore, for
196 equation (1), if we express $Q_{sca}(m, r)$ as $Q_{sca}(m, r) = k \cdot r$, then equation (5) can be expressed
197 as the following:

$$198 \quad \sigma_{sp} = k \cdot \int \pi r^3 n(r) dr \quad (3)$$

199 This explains why $\sigma_{sp}(550 \text{ nm})$ is roughly proportional to $V_a(\text{dry})$. However, the value k varies
200 greatly with particle diameter. The ratio $\sigma_{sp}(550 \text{ nm})/V_a(\text{dry})$ (hereinafter referred to as R_{Vsp}) is
201 mostly affected by the PNSD, which determines the weight of influence different particle
202 diameters have on R_{Vsp} . The discrepancy between the blue line and black line shown in Fig.2a
203 indicates that the fraction of externally mixed BC particles and their sizes has large impact on R_{Vsp} .
204 The difference between the black line and the red line as well as the difference between the solid
205 red line and the dashed red line shown in Fig.2a indicate that the way and the amount of BC mixed
206 with other components also exert significant influences on R_{Vsp} . In summary, the variation of
207 R_{Vsp} is mainly determined by variations in PNSD, mass size distribution and the mixing state of
208 BC. It is difficult to find a simple function describing the relationship between measured σ_{sp} and
209 $V_a(\text{dry})$.

210 Based on PNSD and BC datasets of field campaigns F1 to F6, the relationship between σ_{sp} at
211 550 nm and $V_a(\text{dry})$ of PM_{10} or $\text{PM}_{2.5}$ are simulated using the Mie theory. The results are shown
212 in Fig.3. The results demonstrate that the σ_{sp} at 550 nm is highly correlated with the $V_a(\text{dry})$ of
213 PM_{10} and $\text{PM}_{2.5}$. The square of the correlation coefficient (r^2) between σ_{sp} at 550 nm and $V_a(\text{dry})$
214 of PM_{10} or $\text{PM}_{2.5}$ are 0.94 and 0.99, respectively. A roughly proportional relationship exists

215 between $V_a(\text{dry})$ and $\sigma_{sp}(550 \text{ nm})$, especially for $V_a(\text{dry})$ of $\text{PM}_{2.5}$. However, both R_{Vsp} of
216 PM_{10} and $\text{PM}_{2.5}$ vary significantly. R_{Vsp} of PM_{10} mainly ranges from 2 to 6 $\text{cm}^3/(\mu\text{m}^3 \cdot \text{Mm})$,
217 with an average of 4.2 $\text{cm}^3/(\mu\text{m}^3 \cdot \text{Mm})$. R_{Vsp} of $\text{PM}_{2.5}$ mainly ranges from 3 to 6.5
218 $\text{cm}^3/(\mu\text{m}^3 \cdot \text{Mm})$, with an average of 5.1 $\text{cm}^3/(\mu\text{m}^3 \cdot \text{Mm})$. Simulated size-resolved
219 accumulative contributions to σ_{sp} at 550 nm for all PNSDs measured during campaigns F1 to F6
220 and corresponding size-resolved accumulative contributions to $V_a(\text{dry})$ of PM_{10} are shown in
221 Fig.S2. The results indicate that particles with diameter larger than 2.5 μm usually contribute
222 negligibly to σ_{sp} at 550 nm but contribute about 20% of the total PM_{10} volume. Hence σ_{sp} at 550
223 nm is insensitive to changes in particles mass of diameters between 2.5 to 10 μm . This may
224 partially explain why $V_a(\text{dry})$ of $\text{PM}_{2.5}$ correlates better with σ_{sp} at 550 nm than $V_a(\text{dry})$ of PM_{10} .

225 3.2.2 Machine learning

226 Based on analyses in Sect.3.2.1, R_{Vsp} varies a lot with PNSD being the most dominant
227 influencing factor. The “dry” nephelometer provides not only one single σ_{sp} at 550 nm, it
228 measures six parameters including σ_{sp} and back scattering coefficients (σ_{bsp}) at three wavelengths
229 (for TSI 3563: 450 nm, 550 nm, 700 nm). The Ångström exponent calculated from spectral
230 dependence of σ_{sp} provides information on the mean predominant aerosol size and is associated
231 mostly with PNSD. The variation of the hemispheric backscattering fraction (HBF), which is the
232 ratio between σ_{bsp} and σ_{sp} , is also essentially related to the PNSD. HBFs at three wavelengths
233 (450 nm, 550 nm, 700 nm) and the Ångström exponents calculated from σ_{sp} at different
234 wavelengths (450-550 nm, 550-700 nm, 450-700 nm) for typical non-absorbing aerosol particles
235 with their diameters ranging from 100 nm to 3 μm are simulated using the Mie theory. The results
236 are shown in Fig.4a and Fig.4b. HBF values at three different wavelengths and their differences

237 are more sensitive to changes in PNSD of particle diameters less than about 400 nm. Ångström
238 exponents calculated from σ_{sp} at different wavelengths almost decrease monotonously with
239 particle diameter when particle diameter is less than about 1 μm , however, they differ distinctly
240 when particle diameter is larger than 300 nm. These results indicate that HBFs at three wavelengths
241 and Ångström exponents calculated from σ_{sp} at different wavelengths are sensitive to different
242 diameter ranges of PNSD.

243 Thus, all six parameters measured by the “dry” nephelometer together can provide valuable
244 information about variations in R_{Vsp} . However, no explicit formula exists between these six
245 parameters and $V_a(\text{dry})$. How to use these six optical parameters is a problem. Machine learning
246 methods which can handle many input parameters are capable of learning from historical datasets
247 and then make predictions, and strict relationships among variables are not required. Machine
248 learning methods are powerful tools for tackling highly nonlinear problems and are widely used
249 in different areas. In the light of this, predicting $V_a(\text{dry})$ based on six optical parameters measured
250 by the “dry” nephelometer might be accomplished by using a machine learning method. In this
251 study, random forest is chosen for this purpose.

252 Random forest is a machine learning technique that is widely used for classification and
253 non-linear regression problems (Breiman, 2001). For non-linear regression cases, random forest
254 model consists of an ensemble of binary regression decision trees. Each tree has a randomized
255 training scheme, and an average over the whole ensemble of regression tree predictions is used for
256 final prediction. In this study, the function RandomForestRegressor from the Python Scikit-Learn
257 machine learning library (<http://scikit-learn.org/stable/index.html>) is used. This model has several
258 strengths. First, by averaging over an ensemble of decision trees, there is a significantly lower risk

259 of overfitting. Second, it involves fewer assumptions about the dependence between inputs and
260 outputs when compared with traditional parametric regression models. The random forest model
261 has two parameters: the number of input variables (N_{in}) and the number of trees grown (N_{tree}). In
262 this study, N_{in} and N_{tree} are six and eight, respectively. The six input parameters the three
263 scattering coefficients, three backscattering coefficients.

264 The quality of input datasets is critical to the prediction accuracy of the machine learning
265 method. As discussed in Sect.3.1, modeled σ_{sp} during some field campaigns are not completely
266 consistent with measured σ_{sp} , large bias might exist between them due to the measurement
267 uncertainties of PNSD and σ_{sp} . To avoid that the measurements uncertainties are involved in the
268 training processes of the random forest model. In this study, both the required datasets of six optical
269 parameters which corresponding to measurements of TSI 3563 and $V_a(\text{dry})$ for training the
270 random forest model are calculated or simulated based on measurements of PNSD and BC from
271 field campaigns F1 to F4 and F6. Datasets of PNSD and six optical parameters measured by the
272 nephelometer during campaign F5 are used to verify the prediction ability of the trained random
273 forest model. The performance of this random forest model on predicting both $V_a(\text{dry})$ of PM_{10}
274 and $\text{PM}_{2.5}$ are investigated. A schematic diagram of this method is shown in Fig.5.

275 **3.3 Connecting $f(\text{RH})$ to $V_g(\text{RH})$**

276 **3.3.1 κ -Köhler theory**

277 κ -Köhler theory is used to describe the hygroscopic growth of aerosol particles with different
278 sizes, and the formula expression of κ -Köhler theory can be written as follows (Petters and
279 Kreidenweis, 2007):

280
$$RH = \frac{D^3 - D_d^3}{D^3 - D_d^3(1 - \kappa)} \cdot \exp\left(\frac{4\sigma_{s/a} \cdot M_{water}}{R \cdot T \cdot D_p \cdot g \cdot \rho_w}\right) \quad (4)$$

281 where D is the diameter of the droplet, D_d is the dry diameter, $\sigma_{s/a}$ is the surface tension of
 282 solution/air interface, T is the temperature, M_{water} is the molecular weight of water, R is the
 283 universal gas constant, ρ_w is the density of water, and κ is the hygroscopicity parameter. By
 284 combining the Mie theory and the κ -Köhler theory, both $f(RH)$ and $Vg(RH)$ can be simulated. In
 285 the processes of calculations for modelling $f(RH)$ and $Vg(RH)$, the treatment of BC is same with
 286 those introduced in Sect.2.2. As aerosol particle grow due to aerosol water uptake, the refractive
 287 index will change. In the Mie calculation, impacts of aerosol liquid water on the refractive index
 288 are considered on the basis of volume mixing rule. The used refractive index of liquid water is
 289 $1.33 - 10^{-7}i$ (Seinfeld and Pandis, 2006).

290 **3.3.2 Parameterization schemes for $f(RH)$ and $Vg(RH)$**

291 The $f(RH)$ is defined as $f(RH) = \sigma_{sp}(RH, 550 \text{ nm}) / \sigma_{sp}(dry, 550 \text{ nm})$ where
 292 $\sigma_{sp}(RH, 550 \text{ nm})$ and $\sigma_{sp}(dry, 550 \text{ nm})$ represents σ_{sp} at wavelength 550 nm under certain RH
 293 and dry conditions. Additionally, $Vg(RH)$ is defined as $Vg(RH) = V_a(RH) / V_a(dry)$, where
 294 $V_a(RH)$ represents total volume of aerosol particles under certain RH conditions.

295 A physically based single-parameter representation is proposed by Brock et al. (2016) to
 296 describe $f(RH)$. The parameterization scheme is written as:

297
$$f(RH) = 1 + \kappa_{sca} \frac{RH}{100 - RH} \quad (5)$$

298 where κ_{sca} is the parameter which fits $f(RH)$ best. Here, a brief introduction is given about the
 299 physical understanding of this parameterization scheme. For aerosol particles whose diameters

300 larger than 100 nm, regardless of the kelvin effect, the hygroscopic growth factor for a aerosol
 301 particle can be approximately expressed as $g(RH) \cong (1 + \kappa \frac{RH}{100-RH})^{1/3}$ (Brock et al., 2016).
 302 Enhancement factor in volume can be expressed as the cube of $g(RH)$. Of particular note is that
 303 aerosol particles larger than 100 nm contribute the most to σ_{sp} and $V_a(\text{dry})$, which means that if κ
 304 values of aerosol particles of different sizes are the same, then $Vg(RH)$ can be approximately
 305 expressed as $Vg(RH) = 1 + \kappa \frac{RH}{100-RH}$. In addition, σ_{sp} is usually proportional to $V_a(\text{dry})$ which
 306 indicates that the relative change in σ_{sp} due to aerosol water uptake is roughly proportional to
 307 relative change in aerosol volume. Therefore, $f(RH)$ might also be well described by using the
 308 formula form of equation (5). Previous studies have shown that this parameterization scheme can
 309 describe $f(RH)$ well (Brock et al., 2016;Kuang et al., 2017b).

310 During processes of measuring $f(RH)$, the sample RH in the “dry” nephelometer (RH_0) is
 311 not zero. According to equation (5), the measured $f(RH)_{measure} = \frac{f(RH)}{f(RH_0)}$ should be fitted using
 312 the following formula:

$$313 \quad f(RH)_{measure} = (1 + \kappa_{sca} \frac{RH}{100-RH}) / (1 + \kappa_{sca} \frac{RH_0}{100-RH_0}) \quad (6)$$

314 Based on this equation, κ_{sca} can be calculated from measured $f(RH)$ directly. The typical value of
 315 RH_0 measured in the “dry” nephelometer during Wangdu campaign is about 20%. The importance
 316 of the RH_0 correction changes under different aerosol hygroscopicity and RH_0 conditions. The
 317 parameter κ_{sca} is fitted with and without consideration of RH_0 for $f(RH)$ measurements during
 318 Wangdu campaign, and the results are shown in Fig.S3. The results demonstrate that, overall, the
 319 κ_{sca} will be underestimated if the influence of RH_0 is not considered, and the larger the κ_{sca} the
 320 more that the κ_{sca} will be underestimated.

321 In addition, based on discussions about the physical understanding of equation (5), the
322 $Vg(RH)$ should be well described by the following equation:

$$323 \quad Vg(RH) = 1 + \kappa_{Vf} \frac{RH}{100-RH} \quad (7)$$

324 where κ_{Vf} is the parameter which fits $Vg(RH)$ best. To consolidate this conclusion, a simulative
325 experiment is conducted. In the simulative experiment, average PNSD in dry state and mass
326 concentration of BC during the Haze in China (HaChi) campaign (Kuang et al., 2015) are used.
327 During HaChi campaign, size-resolved κ distributions are derived from measured size-segregated
328 chemical compositions (Liu et al., 2014) and their average is used in this experiment to account
329 the size dependence of aerosol hygroscopicity. Modelled results of $f(RH)$ and $Vg(RH)$ are shown
330 in Fig.7. Results demonstrate that modelled $f(RH)$ and $Vg(RH)$ can be well parameterized using
331 the formula form of equation (5) and (7). Fitted values of κ_{sca} and κ_{Vf} are 0.227 and 0.285,
332 respectively. This result indicates that if linkage between κ_{sca} and κ_{Vf} is established,
333 measurements of $f(RH)$ can be directly related to $Vg(RH)$.

334 3.3.3 Bridge the gap between $f(RH)$ and $Vg(RH)$

335 Many factors have significant influences on the relationships between $f(RH)$ and $Vg(RH)$,
336 such as PNSD, BC mixing state and the size-resolved aerosol hygroscopicity. To gain insights into
337 the relationships between κ_{sca} and κ_{Vf} , a simulative experiment using Mie theory and κ -Köhler
338 theory is designed. In this experiment, all PNSDs at dry state along with mass concentrations of
339 BC from D1 are used, characteristics of these PNSDs can be found in Kuang et al. (2017b). As to
340 size-resolved aerosol hygroscopicity, a number of size-resolved κ distributions were derived from
341 measured size-segregated chemical compositions during HaChi campaign (Liu et al., 2014).

342 Results from other researches also show similar size dependence of aerosol hygroscopicity (Meng
343 et al., 2014). In view of this, the shape of the average size-resolved κ distribution during HaChi
344 campaign (black line shown in Fig.7a) is used in the designed experiment. Other than the shape of
345 size-resolved κ distribution, the overall aerosol hygroscopicity which determines the magnitude
346 of $f(\text{RH})$ also have large impacts on the relationship between κ_{sca} and κ_{Vf} . In view of this, ratios
347 range from 0.05 to 2 with an interval of 0.05 are multiplied with the average size-resolved κ
348 distribution (the black line shown in Fig.7a) to produce a number of size-resolved κ distributions
349 which represent aerosol particles from nearly hydrophobic to highly hygroscopic. During
350 simulating processes, each PNSD is modelled with all produced size-resolved κ distributions. In
351 the following, the ratio κ_{Vf}/κ_{sca} termed as R_{Vf} is used to indicate the relationship between κ_{sca}
352 and κ_{Vf} .

353 In consideration of that values of Ångström exponent contain information about PNSD
354 (Kuang et al., 2017b) and values of κ_{sca} represent overall hygroscopicity of ambient aerosol
355 particles, and both the two parameters can be directly calculated from measurements of a three-
356 wavelength humidified nephelometer system (Kuang et al., 2017b). Simulated R_{Vf} values are
357 spread into a two-dimensional gridded plot. The first dimension is Ångström exponent with an
358 interval of 0.02 and the second dimension is κ_{sca} with an interval of 0.01. Average R_{Vf} value
359 within each grid is represented by color and shown in Fig.6a. Values of Ångström exponent
360 corresponding to used PNSDs are calculated from simultaneously measured σ_{sp} values at 450 nm
361 and 550 nm from TSI 3563 nephelometer. Results shown in Fig.6a exhibit that both PNSD and
362 overall aerosol hygroscopicity have significant influences on R_{Vf} . Simulated values of R_{Vf} range
363 from 0.8 to 1.7 with an average of 1.2. Overall, R_{Vf} value is lower when value of Ångström

364 exponent is larger. With respect to influences of κ_{sca} on R_{Vf} , if Ångström exponent is larger than
365 about 1.1, κ_{sca} have small influences on R_{Vf} while its influence is remarkable when Ångström
366 exponent is lower than 1.1. In addition, the percentile value of standard deviation of R_{Vf} values
367 within each grid divided by its average is shown in Fig.6b. In most cases, these percentile values
368 are less than 10% (about 90%) which demonstrates that R_{Vf} varies little within each grid shown
369 in Fig.6a. This implies that results of Fig.6a can serve as a look up table to estimate R_{Vf} and
370 thereby κ_{Vf} values can be directly predicted from measurements of a three-wavelength humidified
371 nephelometer system.

372 For the look up table shown in Fig.6a, a fixed size-resolved κ distribution is used, which
373 might not be able to capture variations of R_{Vf} induced by different types of size-resolved κ
374 distributions under different PNSD conditions. A simulative experiment is conducted to
375 investigate the performance of this look up table. In this experiment, the following datasets are
376 used: PNSDs and mass concentrations of BC from D1 (the number of used PNSD is 11996), and
377 size-resolved κ distributions from HaChi campaign (Liu et al., 2014) which are presented in Fig.7a
378 (the number is 23). Results shown in Fig.7a imply that the shape of size-resolved κ distribution
379 has no apparent correlation with pollution degrees and varies a lot. During the simulating processes,
380 for each PNSD, it is used to simulate R_{Vf} values corresponding to all used size-resolved κ
381 distributions, therefore, 275908 R_{Vf} values are modelled. Also, modelled values of κ_{sca} and
382 corresponding values of modelled Ångström exponent are together used to estimate R_{Vf} values
383 using the look up table shown in Fig.7a. Results of relative differences between estimated and
384 modelled R_{Vf} values under different pollution conditions are shown in Fig.7b. Overall, 88% of

385 points have absolute relative differences less than 15%, and 68% of points have absolute relative
386 differences less than 10%. This look up table performs better when the air is relatively polluted.

387 **3.4 Calculation of ambient ALWC**

388 According to the equation $V_g(RH) = 1 + \kappa_{Vf} \frac{RH}{100-RH}$, volume concentrations of aerosol
389 liquid water (ALWC) at different RH points can be expressed as:

$$390 \quad ALWC = V_a(\text{dry}) \times (V_g(RH) - 1) = V_a(\text{dry}) \cdot \kappa_{sca} \cdot R_{Vf} \cdot \frac{RH}{100-RH}. \quad (7)$$

391 According to discussions of Sect.3.2, $V_a(\text{dry})$ can be predicted based only on measurements from
392 the “dry” nephelometer by using a random forest model. The training of the random forest model
393 requires only regional historical datasets of simultaneously measured PNSD and BC. The κ_{sca} is
394 directly fitted from $f(RH)$ measurements. The R_{Vf} can be estimated using the look up table
395 introduced in Sect.3.3. Thus, based only on measurements from a three-wavelength humidified
396 nephelometer system, ALWCs of ambient aerosol particles at different RH points can be estimated.
397 If both measurements from the humidified nephelometer system and ambient RH are available,
398 ambient ALWC can be calculated.

399 **4. Results and discussions**

400 **4.1 Validation of the random forest model for predicting $V_a(\text{dry})$ based on measurements of** 401 **the “dry” nephelometer**

402 The machine learning method, random forest model, is proposed to predict $V_a(\text{dry})$ based
403 only on σ_{sp} and σ_{bsp} at three wavelengths measured by the “dry” nephelometer. Datasets of PNSD
404 and BC from field campaigns F1 to F4 and F6 are used to train the random forest model. Datasets

405 of PNSD and optical parameters measured by the “dry” nephelometer from field campaign F5 are
406 used to verify the trained random forest model. The schematic diagram of this method is shown in
407 Fig.5. The comparison results between calculated and predicted $V_a(\text{dry})$ of PM_{10} and $\text{PM}_{2.5}$ are
408 shown in Fig.8. The square of correlation coefficient between predicted and calculated $V_a(\text{dry})$
409 of PM_{10} is 0.96. And almost all points lie between or near 20% relative difference lines. The square
410 of correlation coefficient between predicted and calculated $V_a(\text{dry})$ of $\text{PM}_{2.5}$ is 0.997. And almost
411 all points lie between or near 10% relative difference lines. The standard deviations of relative
412 differences between predicted and calculated $V_a(\text{dry})$ of PM_{10} and $\text{PM}_{2.5}$ are 10% and 4% ,
413 respectively. These results indicate that $V_a(\text{dry})$ of $\text{PM}_{2.5}$ can be well predicted by using the
414 machine learning method. While $V_a(\text{dry})$ of PM_{10} predicted by using the machine learning
415 method has a relatively larger bias.

416 Machine learning methods do not explicitly express relationships between many variables,
417 however, they learn and implicitly construct complex relationships among variables from
418 historical datasets. Many different and comprehensive machine learning methods are developed
419 for diverse applications, and can be directly used as a tool for solving a lot of nonlinear problems
420 which may not be mathematically well understood. We suggest that using machine learning
421 method for estimating $V_a(\text{dry})$ based on measurements of the “dry” nephelometer. The way of
422 estimating $V_a(\text{dry})$ with machine learning method might be applicable for different regions around
423 the world if used estimators are trained with corresponding regional historical datasets.

424 **4.2 Comparison between ambient ALWC calculated from ISORROPIA and measurements**
425 **of the humidified nephelometer system.**

426 So far, widely used tools for prediction of ambient ALWC are thermodynamic models.
427 ISORROPIA-II thermodynamic model (<http://isorrophia.eas.gatech.edu>) is a famous one, and is
428 widely used in researches for predicting pH and ALWC of ambient aerosol particles (Guo et al.,
429 2015; Cheng et al., 2016; Liu et al., 2017). Water soluble ions and gaseous precursors are required
430 as inputs of thermodynamic model. During Gucheng campaign, measurements from both the
431 humidified nephelometer system and IGAC are available. Thus, the ambient ALWC can be
432 calculated through two independent methods: thermodynamic model based on IGAC
433 measurements and the method proposed in Sect.3.4 which is based on measurements of the
434 humidified nephelometer system. In this study, the forward mode in ISORROPIA-II is used, and
435 water-soluble ions in PM_{2.5} and gaseous precursors (NH₃, HNO₃, HCl) measured by the IGAC
436 instrument along with simultaneously measured RH and T are used as inputs. The aerosol water
437 associated with organic matter are not considered in the method of ISORROPIA model, due to the
438 lack of measurements of organic aerosol mass. However, results from previous studies indicate
439 that organic matter induced particle water only account for about 5% of total ALWC (Liu et al.,
440 2017). For the ALWC calculated from the humidified nephelometer system. The needed $V_a(\text{dry})$
441 of PM_{2.5} in equation (7) is calculated from simultaneously measured PNSD.

442 The comparison results between ambient ALWC calculated from these two independent
443 methods are shown in Fig.9a. The square of correlation coefficient between them is 0.92, most of
444 the points lie within or nearby 30% relative difference lines. The slope is 1.14, and the intercept is
445 $-8.6 \mu\text{m}^3/\text{cm}^3$. When ambient RH is higher than 80%, the ambient ALWCs calculated from
446 measurements of the humidified nephelometer system are relatively higher than those calculated
447 based on ISORROPIA- II . When ambient RH is lower than 60%, the ambient ALWCs calculated
448 from measurements of the humidified nephelometer system are relatively lower than those

449 calculated based on ISORROPIA-II. Overall, a good agreement is achieved between ambient
450 ALWC calculated from measurements of the humidified nephelometer system and ISORROPIA
451 thermodynamic model.

452 Guo et al. (2015) conducted the comparison between ambient ALWC calculated from
453 ISORROPIA model and ambient ALWC calculated from measurements of the humidified
454 nephelometer system by assuming $V_g(RH) = f(RH)^{1.5}$. Thus, the comparison results between
455 ambient ALWC calculated based on ISORROPIA and ambient ALWC calculated by assuming
456 $V_g(RH) = f(RH)^{1.5}$ are also shown in Fig.9b. The square of correlation coefficient between them
457 is also 0.92. However, the slope and intercept are 1.7 and $-21 \mu m^3/cm^3$, respectively. When the
458 ambient RH is higher than about 80%, calculated ambient ALWC will be significantly
459 overestimated if assumes that $V_g(RH) = f(RH)^{1.5}$. This method assumes that average scattering
460 efficiency of aerosol particles at dry state and different RH conditions are the same. When ambient
461 RH is high, the particle diameters changes a lot. As the results shown in Fig.S5, for non-absorbing
462 particle, when diameter of aerosol particle in dry state is less than 500 nm, the aerosol scattering
463 efficiency increase almost monotonously with increasing RH especially when RH is higher than
464 80%. Therefore, it is not suitable to assume that average scattering efficiency of aerosol particles
465 at dry state and different RH conditions are the same.

466 **4.3 Volume fractions of ALWC in total ambient aerosol volume**

467 During Wangdu campaign, κ_{sca} ranges from 0.05 to 0.3 with an average of 0.19. Estimated
468 values of R_{Vf} ranges from 0.86 to 1.47, with an average of 1.15. Estimated values of κ_{Vf} ranges
469 from 0.05 to 0.35, with an average of 0.22. The calculated volume fractions of water in total
470 volume of ambient aerosols during Wangdu campaign are shown in Fig.10a. The results indicate

471 that during Wangdu campaign, when ambient RH is higher than 70%, the κ_{Vf} values are relatively
472 higher. The volume fractions of water is always higher than 50% when ambient RH is higher than
473 80%.

474 During Gucheng campaign, κ_{sca} ranges from 0.008 to 0.22 with an average of 0.1, κ_{Vf} ranges
475 from 0.01 to 0.21 with an average of 0.12. The aerosol hygroscopicity during Gucheng campaign
476 is much lower than aerosol hygroscopicity during Wangdu campaign. During Gucheng campaign,
477 the maximum volume fraction of water in ambient aerosol is 42% when ambient RH is at 80%.
478 Averagely speaking, when ambient RH is higher than 90%, the volume fraction of water in ambient
479 aerosols reaches higher than 50%.

480 **4.4 Discussions about the applicability of the proposed method**

481 The method proposed in this research is based on datasets of PNSD, σ_{sp} and size-resolved κ
482 distribution which are measured on the NCP without influences of dust and sea salt. Cautions
483 should be exercised if using the proposed method to estimate the ALWC when the air mass is
484 influenced by sea salt or dust. The way of estimating V_a (dry) with machine learning method might
485 be applicable for different regions around the world. However, the used predictor from machine
486 learning should be trained with corresponding regional historical datasets and PNSD and BC. The
487 way of connecting f (RH) to V_g (RH) might also be applicable for other continental regions. Still,
488 we suggest that the used look up table is simulated from regional historical datasets.

489 Note that the humidified nephelometer usually operates with RH less than 95%. Aerosol
490 water, however, increase dramatically with increasing RH when RH is greater than 95%. Such
491 high RH conditions can occur during the haze events. This may limit the usage of the proposed

492 method when ambient RH is extremely high. As discussed in Sect.3.3, the proposed way of
493 connecting $f(\text{RH})$ and $V_g(\text{RH})$ is based on the κ -Köhler theory. If κ does not change with RH, the
494 proposed method should be applicable when RH is higher than 95%, even the measurements of
495 humidified nephelometer system are conducted when RH is less than 95%. Many studies have
496 done researches about the change of κ with the changing RH (Rastak et al., 2017; Renbaum-Wolff
497 et al., 2016), their results demonstrate that the κ changes with increasing RH. However, few
498 studies have investigated the variation of κ of ambient aerosol particles with changing RH when
499 RH is less than 100%. Liu et al. (2011) have measured κ of ambient aerosol particles at different
500 RHs (90%, 95%, 98.5%) on the NCP. Their results demonstrated that κ at different RHs differ
501 little for ambient aerosol particles with different diameters. Results of Kuang et al. (2017a)
502 indicated that κ values retrieved from $f(\text{RH})$ measurements agree well with κ values at RH of 98%
503 of aerosol particles with diameter of 250 nm. In this respect, the proposed method might be
504 applicable even when ambient RH is extremely high for ambient aerosol particles on the NCP.
505 Moreover, for calculating the ambient ALWC, the measured ambient RH is required. If the
506 ambient RH is higher than 95%, the measured ambient RH with current techniques is highly
507 uncertain. Given this, cautions should be exercised if the ambient ALWC is calculated when the
508 ambient RH is higher than 95%.

509 **5. Conclusions**

510 In this paper, a novel method is proposed to calculate ALWC based on measurements of a
511 three-wavelength humidified nephelometer system. Two critical relationships are required in this
512 method. One is the relationship between $V_a(\text{dry})$ and measurements of the “dry” nephelometer.

513 Another one is the relationship between $V_g(\text{RH})$ and $f(\text{RH})$. The ALWC can be calculated from
514 the estimated $V_a(\text{dry})$ and $V_g(\text{RH})$.

515 Previous studies have shown that an approximate proportional relationship exists between
516 $V_a(\text{dry})$ and corresponding σ_{sp} , especially for fine particles (particle diameter less than 1 μm).
517 However, PNSD and other factors still have significant influences on this proportional relationship.
518 It is difficult to directly estimate $V_a(\text{dry})$ from measured σ_{sp} . In this paper, a random forest
519 predictor from machine learning procedure is used to estimate $V_a(\text{dry})$ based on measurements of
520 a three-wavelength nephelometer. This random forest predictor is trained based on historical
521 datasets of PNSD and BC from several field campaigns conducted on the NCP. This method is
522 then validated using measurements from Wangdu campaign. The square of correlation coefficient
523 between measured and estimated $V_a(\text{dry})$ of PM_{10} and $\text{PM}_{2.5}$ are 0.96 and 0.997, respectively.

524 The relationship between $V_g(\text{RH})$ and $f(\text{RH})$ is investigated in Sect.3 by conducting a
525 simulative experiment. It is found that the complicated relationship between $V_g(\text{RH})$ and $f(\text{RH})$
526 can be disentangled by using a look up table, and parameters required in the look up table can be
527 directly calculated from measurements of a three-wavelength humidified nephelometer system.
528 Given that the $V_a(\text{dry})$ can be estimated from a three-wavelength “dry” nephelometer, the ambient
529 ALWC can be estimated from measurements of a three-wavelength humidified nephelometer
530 system in conjunction with measured ambient RH. We have conducted the comparison between
531 ambient ALWC calculated from ISORROPIA and ambient ALWC calculated from measurements
532 of the humidified nephelometer system. The square of correlation coefficient between them is 0.92,
533 and most of the points lie within or nearby 30% relative difference lines. The slope and intercept
534 are 1.14 and $-8.6 \mu\text{m}^3/\text{cm}^3$, respectively. Overall, a good agreement is achieved between ambient

535 ALWC calculated from measurements of the humidified nephelometer system and ISORROPIA
536 thermodynamic model.

537 Results introduced in this research have bridged the gap between $f(\text{RH})$ and $V_g(\text{RH})$. The
538 advantage of using measurements of a humidified nephelometer system to estimate ALWC is that
539 this technique has a fast response time and can provide continuous measurements of the changing
540 ambient conditions. The new method proposed in this research will facilitate the real-time
541 monitoring of the ambient ALWC and further our understanding of roles of ALWC in atmospheric
542 chemistry, secondary aerosol formation and climate change.

543 **Acknowledgments**

544 This work is supported by the National Natural Science Foundation of China (41590872 and
545 41505107) and the National Key R&D Program of China (2016YFC020000: Task 5).

546 **References**

- 547 Anderson, T., Covert, D., Marshall, S., Laucks, M., Charlson, R., Waggoner, A., Ogren, J., Caldow,
548 R., Holm, R., and Quant, F.: Performance characteristics of a high-sensitivity, three-wavelength,
549 total scatter/backscatter nephelometer, *Journal of Atmospheric and Oceanic Technology*, 13, 967-
550 986, 1996.
- 551 Anderson, T. L., and Ogren, J. A.: Determining aerosol radiative properties using the TSI 3563
552 integrating nephelometer, *Aerosol Science and Technology*, 29, 57-69,
553 10.1080/02786829808965551, 1998.
- 554 Bian, Y. X., Zhao, C. S., Ma, N., Chen, J., and Xu, W. Y.: A study of aerosol liquid water content
555 based on hygroscopicity measurements at high relative humidity in the North China Plain, *Atmos.*
556 *Chem. Phys.*, 14, 6417-6426, 10.5194/acp-14-6417-2014, 2014.
- 557 Birmili, W., Stratmann, F., and Wiedensohler, A.: Design of a DMA-based size spectrometer for a
558 large particle size range and stable operation, *Journal of Aerosol Science*, 30, 549-553,
559 10.1016/s0021-8502(98)00047-0, 1999.
- 560 Bohren, C. F., and Huffman, D. R.: *Absorption and scattering of light by small particles*, Wiley,
561 New York, USA, 2008.
- 562 Breiman, L.: Random forests, *Machine Learning*, 45, 5-32, 10.1023/a:1010933404324, 2001.
- 563 Brock, C. A., Wagner, N. L., Anderson, B. E., Attwood, A. R., Beyersdorf, A., Campuzano-Jost,
564 P., Carlton, A. G., Day, D. A., Diskin, G. S., Gordon, T. D., Jimenez, J. L., Lack, D. A., Liao, J.,

565 Markovic, M. Z., Middlebrook, A. M., Ng, N. L., Perring, A. E., Richardson, M. S., Schwarz, J. P.,
566 Washenfelder, R. A., Welti, A., Xu, L., Ziemba, L. D., and Murphy, D. M.: Aerosol optical
567 properties in the southeastern United States in summer – Part 1: Hygroscopic growth, *Atmos.*
568 *Chem. Phys.*, 16, 4987-5007, 10.5194/acp-16-4987-2016, 2016.

569 Cheng, Y., Zheng, G., Wei, C., Mu, Q., Zheng, B., Wang, Z., Gao, M., Zhang, Q., He, K.,
570 Carmichael, G., Pöschl, U., and Su, H.: Reactive nitrogen chemistry in aerosol water as a source
571 of sulfate during haze events in China, *Science Advances*, 2, 10.1126/sciadv.1601530, 2016.

572 Covert, D. S., Charlson, R., and Ahlquist, N.: A study of the relationship of chemical composition
573 and humidity to light scattering by aerosols, *Journal of applied meteorology*, 11, 968-976, 1972.

574 Drinovec, L., Močnik, G., Zotter, P., Prévôt, A. S. H., Ruckstuhl, C., Coz, E., Rupakheti, M., Sciare,
575 J., Müller, T., Wiedensohler, A., and Hansen, A. D. A.: The "dual-spot" Aethalometer: an improved
576 measurement of aerosol black carbon with real-time loading compensation, *Atmospheric*
577 *Measurement Techniques*, 8, 1965-1979, 10.5194/amt-8-1965-2015, 2015.

578 Engelhart, G. J., Hildebrandt, L., Kostenidou, E., Mihalopoulos, N., Donahue, N. M., and Pandis,
579 S. N.: Water content of aged aerosol, *Atmos. Chem. Phys.*, 11, 911-920, 10.5194/acp-11-911-2011,
580 2011.

581 Fierz-Schmidhauser, R., Zieger, P., Vaishya, A., Monahan, C., Bialek, J., O'Dowd, C. D., Jennings,
582 S. G., Baltensperger, U., and Weingartner, E.: Light scattering enhancement factors in the marine
583 boundary layer (Mace Head, Ireland), *Journal of Geophysical Research: Atmospheres*, 115,
584 D20204, 10.1029/2009JD013755, 2010.

585 Guo, H., Xu, L., Bougiatioti, A., Cerully, K. M., Capps, S. L., Hite Jr, J. R., Carlton, A. G., Lee, S.
586 H., Bergin, M. H., Ng, N. L., Nenes, A., and Weber, R. J.: Fine-particle water and pH in the
587 southeastern United States, *Atmos. Chem. Phys.*, 15, 5211-5228, 10.5194/acp-15-5211-2015, 2015.

588 Kuang, Y., Zhao, C. S., Tao, J. C., and Ma, N.: Diurnal variations of aerosol optical properties in
589 the North China Plain and their influences on the estimates of direct aerosol radiative effect, *Atmos.*
590 *Chem. Phys.*, 15, 5761-5772, 10.5194/acp-15-5761-2015, 2015.

591 Kuang, Y., Zhao, C. S., Tao, J. C., Bian, Y. X., and Ma, N.: Impact of aerosol hygroscopic growth
592 on the direct aerosol radiative effect in summer on North China Plain, *Atmospheric Environment*,
593 147, 224-233, <http://dx.doi.org/10.1016/j.atmosenv.2016.10.013>, 2016.

594 Kuang, Y., Zhao, C., Tao, J., Bian, Y., Ma, N., and Zhao, G.: A novel method for deriving the
595 aerosol hygroscopicity parameter based only on measurements from a humidified nephelometer
596 system, *Atmos. Chem. Phys.*, 17, 6651-6662, 10.5194/acp-17-6651-2017, 2017a.

597 Kuang, Y., Zhao, C., Tao, J., Bian, Y., Ma, N., and Zhao, G.: A novel method to derive the aerosol
598 hygroscopicity parameter based only on measurements from a humidified nephelometer system,
599 *Atmos. Chem. Phys. Discuss.*, 2017, 1-25, 10.5194/acp-2016-1066, 2017b.

600 Liu, H. J., Zhao, C. S., Nekat, B., Ma, N., Wiedensohler, A., van Pinxteren, D., Spindler, G., Müller,
601 K., and Herrmann, H.: Aerosol hygroscopicity derived from size-segregated chemical composition
602 and its parameterization in the North China Plain, *Atmos. Chem. Phys.*, 14, 2525-2539,
603 10.5194/acp-14-2525-2014, 2014.

604 Liu, M., Song, Y., Zhou, T., Xu, Z., Yan, C., Zheng, M., Wu, Z., Hu, M., Wu, Y., and Zhu, T.: Fine
605 particle pH during severe haze episodes in northern China, *Geophys. Res. Lett.*, 44, 5213-5221,
606 10.1002/2017GL073210, 2017.

607 Liu, P. F., Zhao, C. S., Göbel, T., Hallbauer, E., Nowak, A., Ran, L., Xu, W. Y., Deng, Z. Z., Ma,
608 N., Mildenberger, K., Henning, S., Stratmann, F., and Wiedensohler, A.: Hygroscopic properties
609 of aerosol particles at high relative humidity and their diurnal variations in the North China Plain,
610 *Atmos. Chem. Phys.*, 11, 3479-3494, 10.5194/acp-11-3479-2011, 2011.

611 Ma, N., Zhao, C. S., Müller, T., Cheng, Y. F., Liu, P. F., Deng, Z. Z., Xu, W. Y., Ran, L., Nekat, B.,
612 van Pinxteren, D., Gnauk, T., Müller, K., Herrmann, H., Yan, P., Zhou, X. J., and Wiedensohler,
613 A.: A new method to determine the mixing state of light absorbing carbonaceous using the
614 measured aerosol optical properties and number size distributions, *Atmos. Chem. Phys.*, 12, 2381-
615 2397, 10.5194/acp-12-2381-2012, 2012.

616 Martin, S. T.: Phase Transitions of Aqueous Atmospheric Particles, *Chem. Rev.*, 100, 3403-3454,
617 10.1021/cr990034t, 2000.

618 Meier, J., Wehner, B., Massling, A., Birmili, W., Nowak, A., Gnauk, T., Brüggemann, E., Herrmann,
619 H., Min, H., and Wiedensohler, A.: Hygroscopic growth of urban aerosol particles in Beijing
620 (China) during wintertime: a comparison of three experimental methods, *Atmos. Chem. Phys.*, 9,
621 6865-6880, 10.5194/acp-9-6865-2009, 2009.

622 Meng, J. W., Yeung, M. C., Li, Y. J., Lee, B. Y. L., and Chan, C. K.: Size-resolved cloud
623 condensation nuclei (CCN) activity and closure analysis at the HKUST Supersite in Hong Kong,
624 *Atmos. Chem. Phys.*, 14, 10267-10282, 10.5194/acp-14-10267-2014, 2014.

625 Petters, M. D., and Kreidenweis, S. M.: A single parameter representation of hygroscopic growth
626 and cloud condensation nucleus activity, *Atmospheric Chemistry and Physics*, 7, 1961-1971, 2007.

627 Pinnick, R. G., Jennings, S. G., and Chýlek, P.: Relationships between extinction, absorption,
628 backscattering, and mass content of sulfuric acid aerosols, *Journal of Geophysical Research:*
629 *Oceans*, 85, 4059-4066, 10.1029/JC085iC07p04059, 1980.

630 Rader, D. J., and McMurry, P. H.: Application of the tandem differential mobility analyzer to
631 studies of droplet growth or evaporation, *Journal of Aerosol Science*, 17, 771-787,
632 [http://dx.doi.org/10.1016/0021-8502\(86\)90031-5](http://dx.doi.org/10.1016/0021-8502(86)90031-5), 1986.

633 Rastak, N., Pajunoja, A., Acosta Navarro, J. C., Ma, J., Song, M., Partridge, D. G., Kirkevåg, A.,
634 Leong, Y., Hu, W. W., Taylor, N. F., Lambe, A., Cerully, K., Bougiatioti, A., Liu, P., Krejci, R.,
635 Petäjä, T., Percival, C., Davidovits, P., Worsnop, D. R., Ekman, A. M. L., Nenes, A., Martin, S.,
636 Jimenez, J. L., Collins, D. R., Topping, D. O., Bertram, A. K., Zuend, A., Virtanen, A., and Riipinen,
637 I.: Microphysical explanation of the RH-dependent water affinity of biogenic organic aerosol and
638 its importance for climate, *Geophys. Res. Lett.*, 44, 5167-5177, 10.1002/2017GL073056, 2017.

639 Renbaum-Wolff, L., Song, M., Marcolli, C., Zhang, Y., Liu, P. F., Grayson, J. W., Geiger, F. M.,
640 Martin, S. T., and Bertram, A. K.: Observations and implications of liquid-liquid phase separation
641 at high relative humidities in secondary organic material produced by α -pinene ozonolysis without
642 inorganic salts, *Atmos. Chem. Phys.*, 16, 7969-7979, 10.5194/acp-16-7969-2016, 2016.

643 Seinfeld, J. H., and Pandis, S. N.: *Atmospheric chemistry and physics: from air pollution to climate*
644 *change*, John Wiley & Sons, 2006.

645 Sherman, J. P., Sheridan, P. J., Ogren, J. A., Andrews, E., Hageman, D., Schmeisser, L., Jefferson,
646 A., and Sharma, S.: A multi-year study of lower tropospheric aerosol variability and systematic
647 relationships from four North American regions, *Atmos. Chem. Phys.*, 15, 12487-12517,
648 10.5194/acp-15-12487-2015, 2015.

649 Tao, J. C., Zhao, C. S., Ma, N., and Liu, P. F.: The impact of aerosol hygroscopic growth on the
650 single-scattering albedo and its application on the NO₂ photolysis rate coefficient, *Atmos. Chem.*
651 *Phys.*, 14, 12055-12067, 10.5194/acp-14-12055-2014, 2014.

652 Wang, G., Zhang, R., Gomez, M. E., Yang, L., Levy Zamora, M., Hu, M., Lin, Y., Peng, J., Guo,
653 S., Meng, J., Li, J., Cheng, C., Hu, T., Ren, Y., Wang, Y., Gao, J., Cao, J., An, Z., Zhou, W., Li, G.,
654 Wang, J., Tian, P., Marrero-Ortiz, W., Secret, J., Du, Z., Zheng, J., Shang, D., Zeng, L., Shao, M.,
655 Wang, W., Huang, Y., Wang, Y., Zhu, Y., Li, Y., Hu, J., Pan, B., Cai, L., Cheng, Y., Ji, Y., Zhang,
656 F., Rosenfeld, D., Liss, P. S., Duce, R. A., Kolb, C. E., and Molina, M. J.: Persistent sulfate

657 formation from London Fog to Chinese haze, Proc Natl Acad Sci U S A, 10.1073/pnas.1616540113,
 658 2016.
 659 Wex, H., Neususs, C., Wendisch, M., Stratmann, F., Koziar, C., Keil, A., Wiedensohler, A., and
 660 Ebert, M.: Particle scattering, backscattering, and absorption coefficients: An in situ closure and
 661 sensitivity study, Journal of Geophysical Research-Atmospheres, 107, 18, 10.1029/2000jd000234,
 662 2002.
 663 Wu, Z. J., Zheng, J., Shang, D. J., Du, Z. F., Wu, Y. S., Zeng, L. M., Wiedensohler, A., and Hu, M.:
 664 Particle hygroscopicity and its link to chemical composition in the urban atmosphere of Beijing,
 665 China, during summertime, Atmos. Chem. Phys., 16, 1123-1138, 10.5194/acp-16-1123-2016,
 666 2016.
 667 Zieger, P., Fierz-Schmidhauser, R., Gysel, M., Ström, J., Henne, S., Yttri, K. E., Baltensperger, U.,
 668 and Weingartner, E.: Effects of relative humidity on aerosol light scattering in the Arctic, Atmos.
 669 Chem. Phys., 10, 3875-3890, 10.5194/acp-10-3875-2010, 2010.
 670

671

672

673

674

675 Table 1 Abbreviations

RH	relative humidity
PM _{2.5}	particulate matter with aerodynamic diameter of less than 2.5 μm
PM ₁₀	particulate matter with aerodynamic diameter of less than 10 μm
<i>f</i> (RH)	aerosol light scattering enhancement factor at 550 nm
ALWC	aerosol liquid water content: volume concentrations of water in ambient aerosols
<i>V_a</i> (dry)	total volume of ambient aerosol particles in dry state
<i>V_g</i> (RH)	aerosol volume enhancement factor due to water uptake
NCP	North China Plain
HTDMA	humidified tandem differential mobility analyser system
PNSD	particle number size distribution
BC	black carbon
<i>g</i> (RH)	hygroscopic growth factor
APS	Aerodynamic Particle Sizer
SMPS	scanning mobility particle size spectrometer

σ_{sp}	aerosol light scattering coefficient
σ_{bsp}	aerosol back scattering coefficient
σ_{ext}	aerosol extinction coefficient
R_{Vsp}	$\sigma_{sp}(550\text{ nm})/V_a(\text{dry})$
F1 to F6	referred as to five field campaigns listed in Table 2
D1	PNSD, BC and nephelometer measurements from F2, F4 and F5

676

677

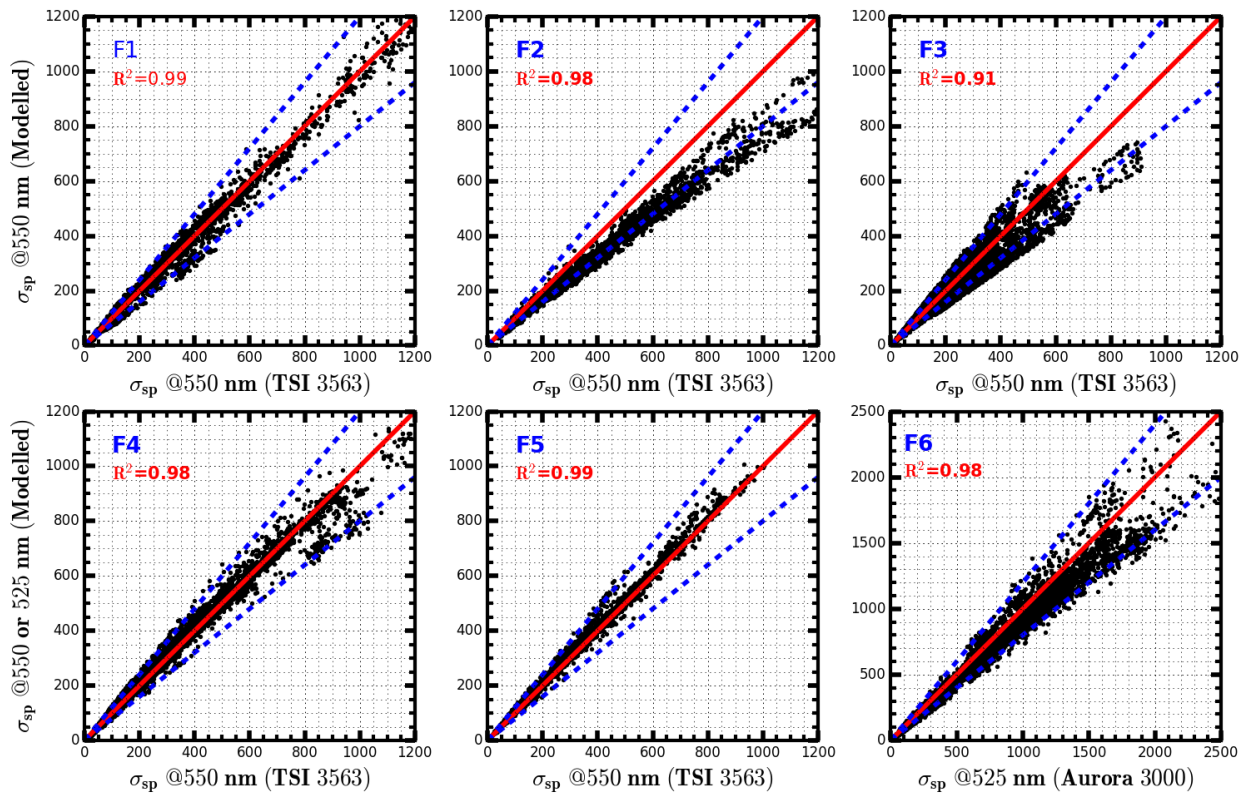
678

679 **Table 2.** Locations, time periods and used datasets of six field campaigns

Location	Wuqing	Wuqing	Xianghe	Xianghe	Wangdu	Gucheng
Time period	7 march to 4 April, 2009	12 July to 14 August, 2009	22 July to 30 August, 2012	9 July to 8 August, 2013	4 June to 14 July, 2014	15 October to 25 November, 2016
PNSD	TSMPS+APS	TSMPS+APS	SMPS+APS	TSMPS+APS	TSMPS+APS	SMPS+APS
BC	MAAP	MAAP	MAAP	MAAP	MAAP	AE33
σ_{sp}	TSI 3563	TSI 3563	TSI 3563	TSI 3563	TSI 3563	Aurora 3000
$f(\text{RH})$					Humidified nephelometer system	Humidified nephelometer system
Water soluble Ions						IGAC
Campaign Name	F1	F2	F3	F4	F5	F6

680

681



682

683 **Figure 1.** Comparisons between measured and calculated σ_{sp} , solid red lines are 1:1 references lines. Dashed
 684 blue lines are 20% relative difference lines. R^2 is square of correlation coefficient between measured and
 685 modelled σ_{sp} . Blue texts at the upper left corners are corresponding field campaigns as listed in Table2.
 686

687

688

689

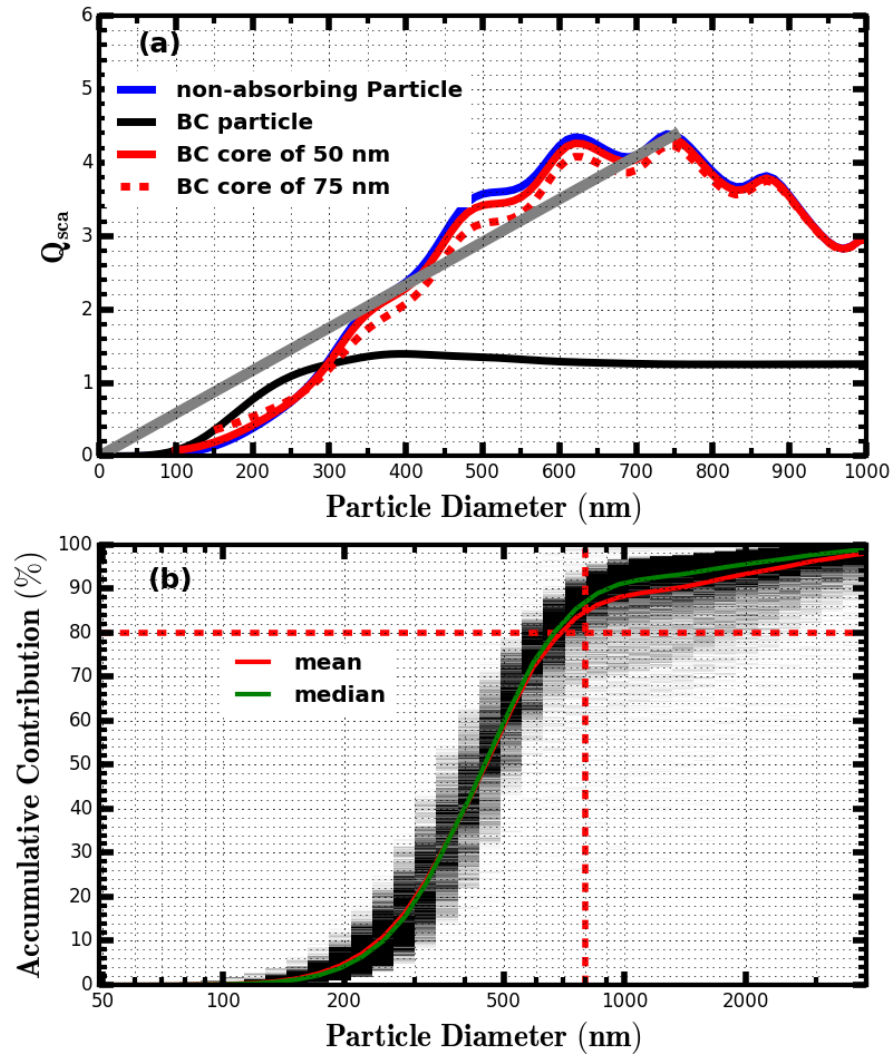
690

691

692

693

694

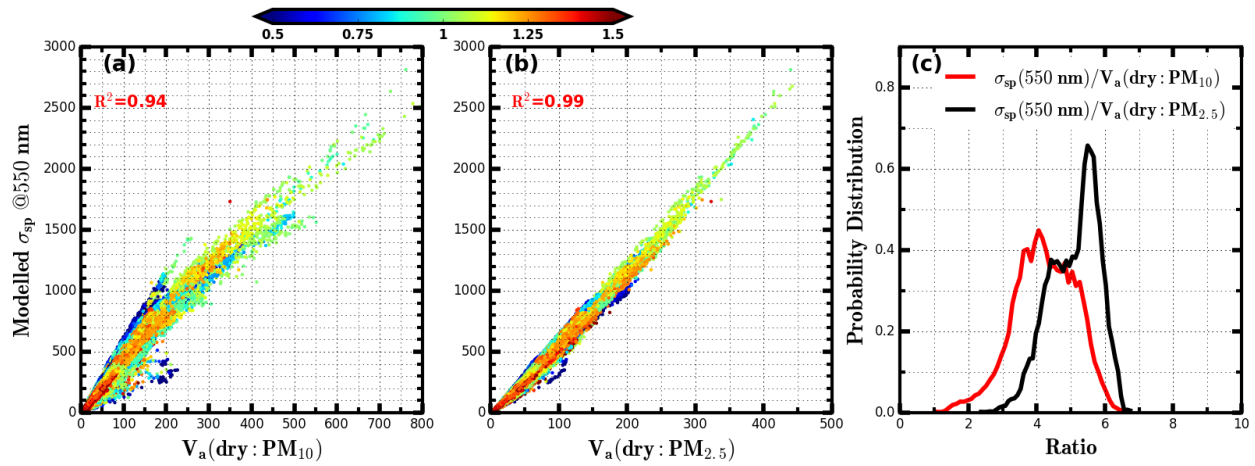


695

696 **Figure 2.** (a) Q_{sca} at 550 nm as a function of particle diameter for four types of aerosol particles: almost non-
697 absorbing aerosol particle, BC particle, BC particle core-shell mixed with non-absorbing components and the
698 radius of inner BC core are 50 nm and 70 nm. The gray line corresponds to the fitted linear line for the case of
699 non-absorbing particle when particle diameter is less than 750 nm. (b) Simulated size-resolved accumulative
700 contribution to σ_{sp} at 550 nm for all PNSDs measured during Wangdu campaign, the color scales (from light
701 gray to black) represent occurrences. The dashed dotted lines in (b) represents the position of 800 nm and 80%
702 contribution, respectively.

703

704



705

706 **Figure 3.** (a) and (b): Modelled σ_{sp} at 550 nm based on PNSD and BC versus $V_a(\text{dry})$ of PM_{10} or $\text{PM}_{2.5}$
707 calculated from measured PNSD. PNSD and BC datasets from six field campaigns listed in Table 2 are used.
708 The unit of $V_a(\text{dry})$ is $\mu\text{m}^3/\text{cm}^3$, the unit of σ_{sp} is Mm^{-1} . Colors of scattered points in (a) and (b) represent
709 corresponding values of Ångström exponent. R^2 is the square of correlation coefficient. (c) The probability
710 distribution of the modelled ratio between σ_{sp} at 550 nm and $V_a(\text{dry})$ of PM_{10} or $\text{PM}_{2.5}$.

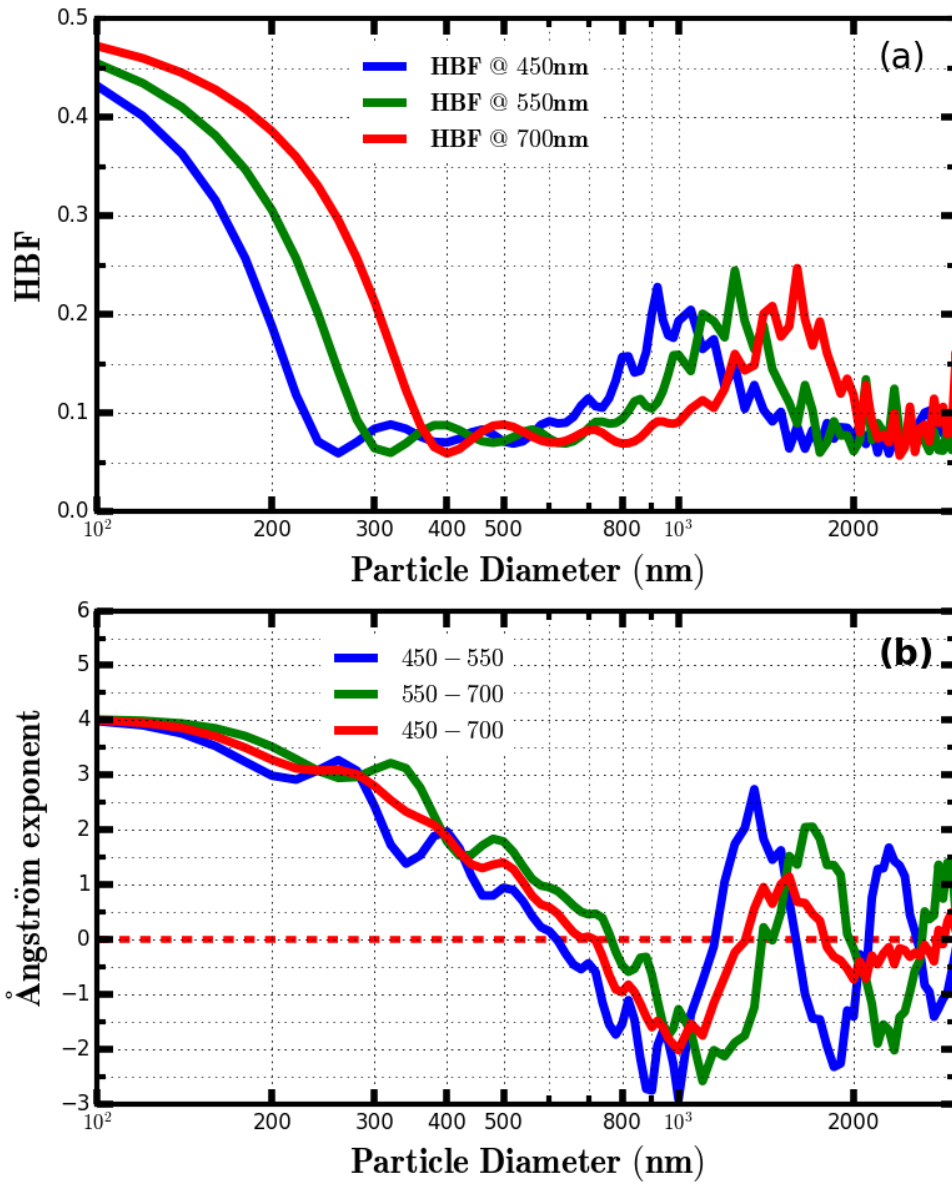
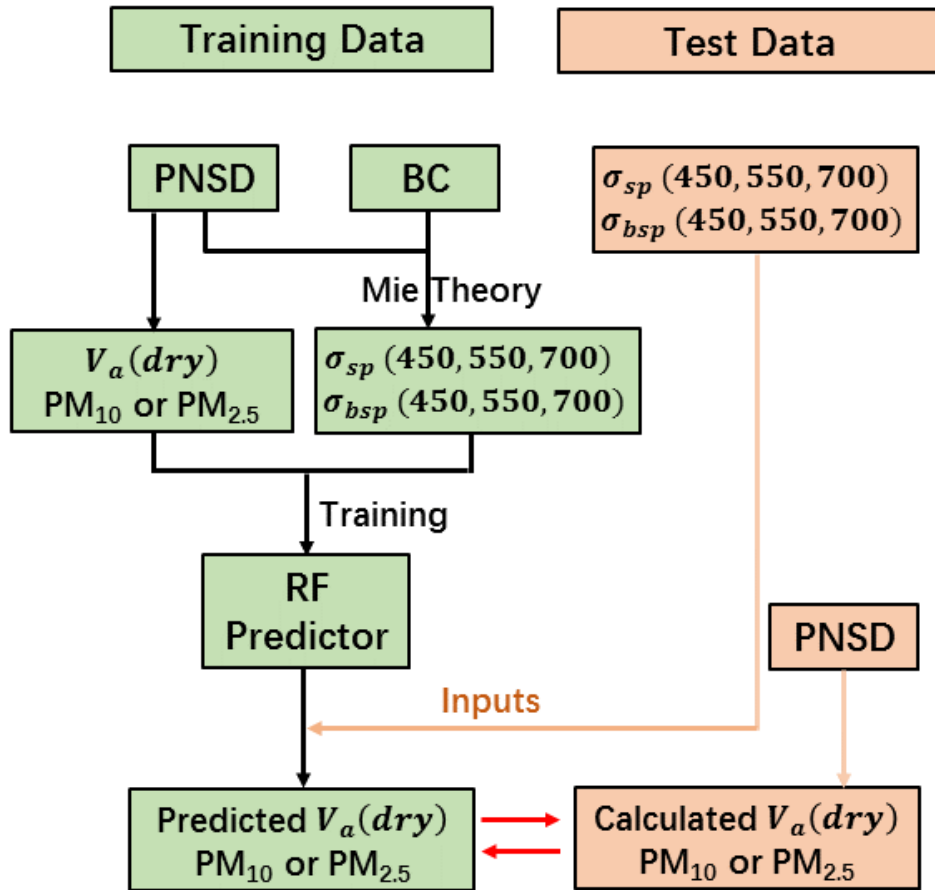


Figure 4. (a) Simulated HBF at three wavelengths as a function particle diameter. (b) Simulated Ångström exponent values as a function a particle diameter.

711
 712
 713
 714
 715
 716
 717
 718
 719



720

721 **Figure 5.** Schematic diagram of training the random forest (RF) model and verifying the performance of trained
 722 RF predictor. The trained datasets of PNSD and BC are from field campaigns F1 to F4 and F6, the test datasets
 723 of PNSD and optical parameters are from campaign F5, σ_{bsp} is the back scattering coefficient.

724

725

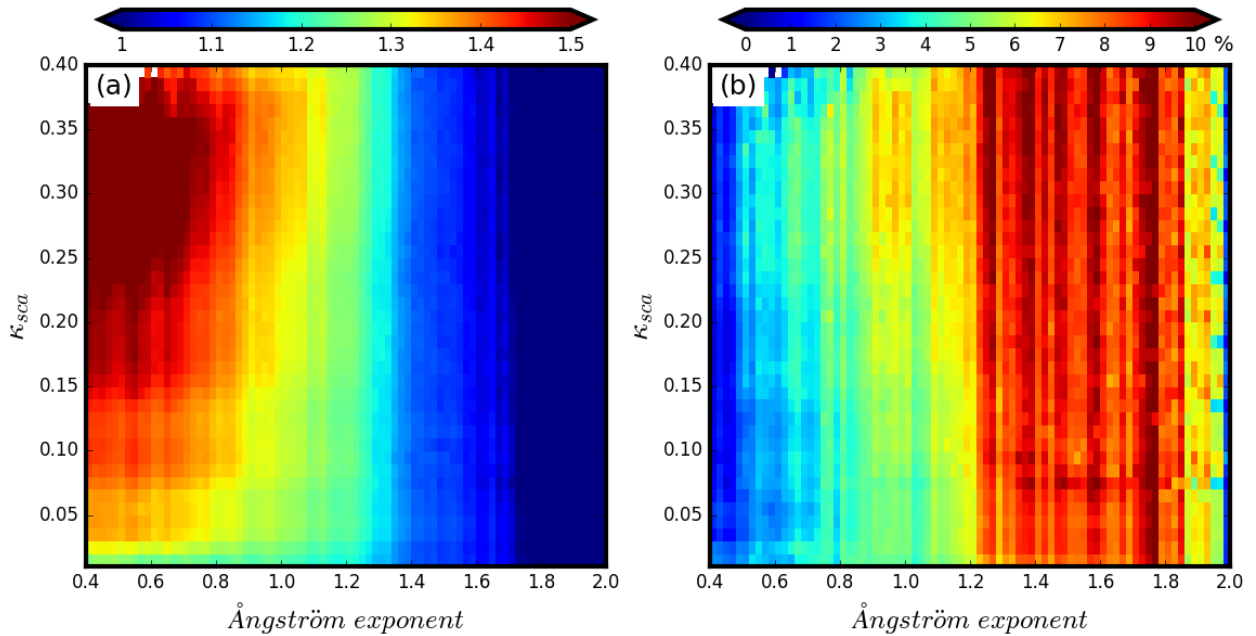
726

727

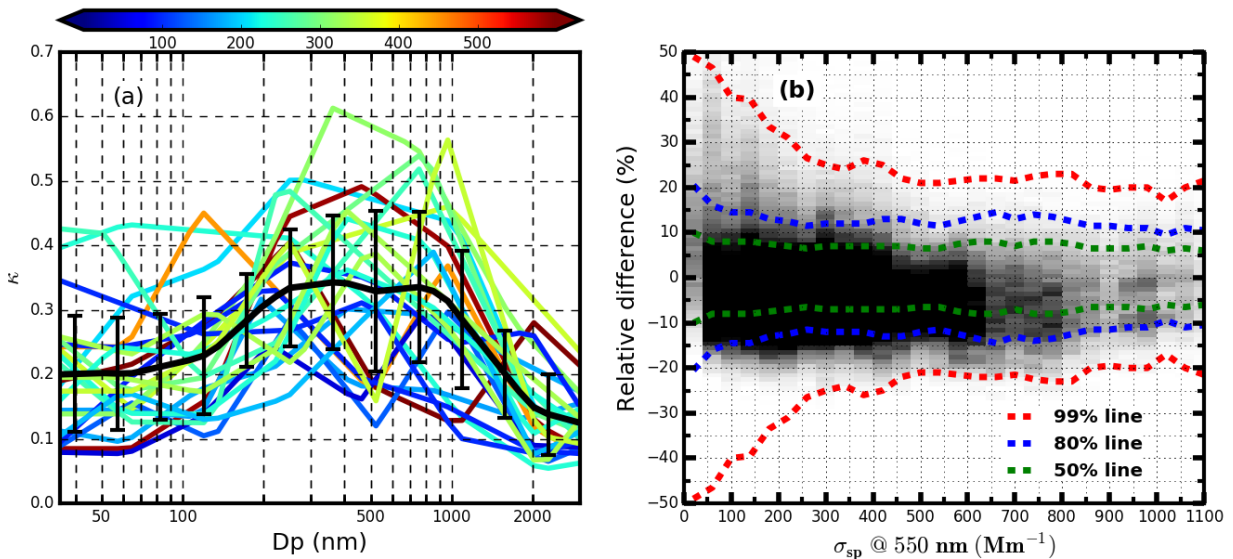
728

729

730



731
 732 **Figure 6.** (a) Colors represent R_{Vf} values and the colorbar is shown on the top of this figure, x-axis represents
 733 Ångström exponent and y-axis represents κ_{sca} . (b) Meanings of x-axis and y-axis are same with them in (a),
 734 however, color represents the percentile value of the standard deviation of R_{Vf} values within each grid divided
 735 by their average.
 736

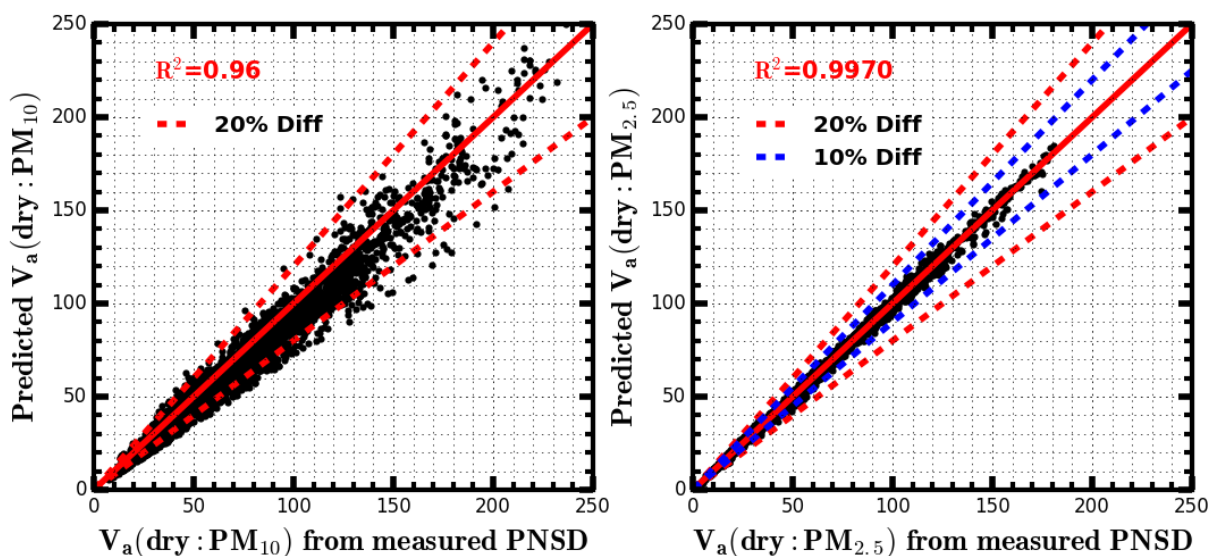


737
 738 **Figure 7.** (a) All size-resolved κ distributions which are derived from measured size-segregated chemical
 739 compositions during HaChi campaign, colors represent corresponding values of average σ_{sp} at 550 nm (Mm^{-1}),
 740 black solid line is the average size-resolved κ distribution and error bars are standard deviations ; (b) The gray

741 colors represent the distribution of relative differences between modelled and estimated R_{Vf} values, darker grids
742 have higher frequency, dashed lines with the same color mean that corresponding percentile of points locate
743 between the two lines.

744

745



746

747 **Figure 8.** The comparison between $V_a(\text{dry})$ of PM_{10} or $\text{PM}_{2.5}$ calculated from measured PNSD and $V_a(\text{dry})$ of
748 PM_{10} or $\text{PM}_{2.5}$ which are predicted based on six optical parameters measured by the “dry” nephelometer
749 by using the random forest model. The unit of $V_a(\text{dry})$ is $\mu\text{m}^3/\text{cm}^3$. R^2 is the square of correlation coefficient.
750 Solid red line is the 1:1 line, dashed red lines and dashed blue lines represent 20% and 10% relative difference
751 lines.

752

753

754

755

756

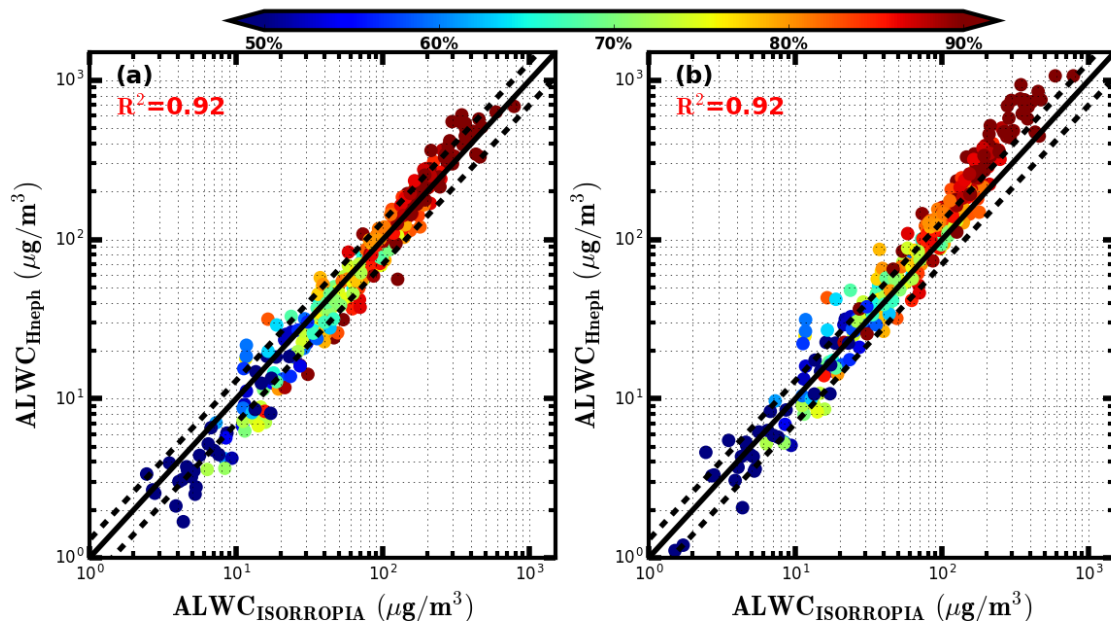
757

758

759

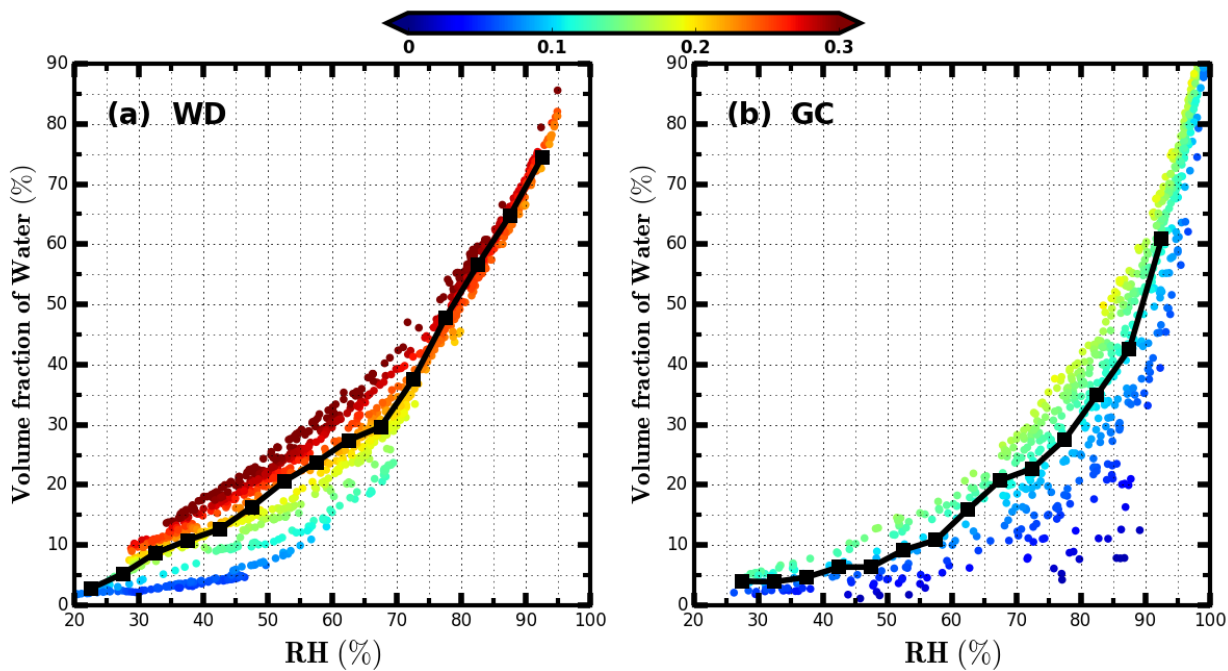
760

761



762

763 **Figure 9.** The comparison between ALWC calculated from ISORROPIA thermodynamic model ($ALWC_{ISORROPIA}$)
 764 and ALWC calculated from measurements of the humidified nephelometer system ($ALWC_{Hneph}$). The black solid
 765 line is the 1:1 line, the two dashed black lines are 30% relative difference lines. R^2 is the square of correlation
 766 coefficient. Colors of scatter points represent ambient RH. (a) $ALWC_{Hneph}$ is calculated using the method
 767 proposed in this research. (b) $ALWC_{Hneph}$ is calculated by assuming $Vg(RH)=f(RH)^{1.5}$ (Guo et al., 2015).
 768



769

770 **Figure 10.** Volume fractions of water in total volume of ambient aerosols during Wangdu (WD) and Gucheng

771 (GC) campaigns. X-axis represents measured ambient RH. Y-axis represents volume fractions of water. Colors
772 of scatter points represent corresponding κ_{vf} . Black solid lines in (a) and (b) show the average volume
773 fractions of water under different ambient RH conditions.
774

775

776

777

778

779

780

781